

A Laser Synthesis Route to Boron-Doped Gold Nanoparticles Designed for X-Ray Radiotherapy and Boron Neutron Capture Therapy Assisted by CT Imaging

Stefano Scaramuzza, Clara M.G. de Faria, Vito Coviello, Daniel Forrer, Luca Artiglia, Denis Badocco, Paolo Pastore, Paolo Ghigna, Ian Postuma, Laura Cansolino, Cinzia Ferrari, Silva Bortolussi, Riccardo Vago, Antonello E. Spinelli, Marina Bekić, Miodrag Čolić, and Vincenzo Amendola*

New multifunctional theranostic vectors allow the expansion of cancer therapeutic approaches toward scarcely investigated fields. One example is the combination of boron neutron capture therapy (BNCT) and X-ray radiotherapy (XRT) for treating normal and XRT-resistant hypoxic tumor regions and reduce recurrence. Of great relevance for BNCT is also the support of viable, rapid, safe, and reliable techniques for the localization and quantification of the radiosensitizers in the tissues. To address these challenges, polymer-coated Au-B nanoparticles (NPs) are obtained starting from a laser ablation in liquid process. Despite thermodynamic constraints, the two elements coexist by short-range boron segregation in the gold lattice, as demonstrated experimentally and explained with the support of density functional theory calculations. Thus, the Au-B NPs maintain a marked gold character such as biocompatibility, stability, and straightforward surface chemistry with thiolated compounds, desirable for the integration with agents capable of cell targeting and internalization. Overall, the Au-B NPs exhibit the appropriate features for the investigation of combined BNCT and XRT, supported by the localization and quantification with X-ray computed tomography imaging. Besides, the Au-B nanotechnology tool is achievable without renouncing to reproducibility, environmental sustainability, and cost affordability thanks to the laser-assisted synthetic pathway.

1. Introduction


Nanomedicine is bringing several innovations to healthcare through the development of a wide set of nanostructures for clinical treatments and bioanalytical procedures.^[1,2] The key advantages of nanostructures are in the better properties and performances compared to conventional medical technologies, but also critically rely upon the superior flexibility for tailoring multiple features toward a specific application, as well as the possibility of introducing multiple functions which are traditionally covered only with diverse compounds.^[2–4] Hence, the progress of nanomedicine requires the continuous exploration of the multiple possibilities available through the combination of inorganic, organic, and biological nanostructured components aiming to the improvement of medical technologies.^[1,3,5,6] In this context, nanoalloys are in the spotlight as powerful and versatile materials for the integration of various functionalities in a

S. Scaramuzza, C. M. de Faria, V. Coviello, D. Forrer, L. Artiglia, D. Badocco, P. Pastore, V. Amendola
Department of Chemical Sciences
University of Padova
Via Marzolo 1, Padova 35131, Italy
E-mail: vincenzo.amendola@unipd.it

D. Forrer
CNR – ICMATE
Padova 35131, Italy
P. Ghigna
Department of Chemistry
University of Pavia
and Unità INSTM di Pavia
V.le Taramelli 13, Pavia 27100, Italy

I. Postuma, L. Cansolino, C. Ferrari, S. Bortolussi
INFN (National Institute of Nuclear Physics) Pavia
Via Bassi 6, Pavia 27100, Italy

L. Cansolino, C. Ferrari
Department of Clinical Surgical Sciences
Integrated unit of experimental surgery
advanced microsurgery and regenerative medicine
University of Pavia
Pavia 27100, Italy

 The ORCID identification number(s) for the author(s) of this article can be found under <https://doi.org/10.1002/adfm.202303366>

© 2023 The Authors. Advanced Functional Materials published by Wiley-VCH GmbH. This is an open access article under the terms of the Creative Commons Attribution-NonCommercial License, which permits use, distribution and reproduction in any medium, provided the original work is properly cited and is not used for commercial purposes.

DOI: 10.1002/adfm.202303366

single nanomedicine. For instance, Pt-Cu NPs were used for photothermal therapy as well as photoacoustic imaging and drug release.^[7] Also, Pt-Co NPs were exploited as efficient contrast agents for photoacoustic imaging and magnetic resonance imaging (MRI), with the ability to guide laser irradiation for photothermal therapy.^[8] Au-Ag NPs were used as radiosensitizers for X-rays and gamma-rays, also showing the potential for microenvironment-activated generation of reactive oxygen species.^[9–11] Magneto-plasmonic Au-Fe alloy NPs proved to be an effective multimodal contrast agent for X-ray computed tomography (CT), MRI, and Raman imaging.^[12] Transformable equimolar Au-Fe nanoalloys can act as bimodal contrast agents for CT and MRI and, after use, they can spontaneously dissolve in vivo,^[13] solving the nanomedicine dilemma of NPs biopersistence versus optimal biodistribution.^[5,13,14] Biodegradability was observed also in MRI contrast agents made of polymer-coated silver-iron nanoparticles.^[15] and in liquid Ga eutectics used for drug delivery.^[16] Nonetheless, nanoalloys remain poorly investigated compared to other nanosystems such as a single element or polymeric nanoparticles, core-shells, heterostructures, and liposomes.^[1,3,17,18]

Radiotherapy is a field where nanoalloys can enable unprecedented possibilities through the development of sensitizers for complementary radiation types.^[4,19] This is even more advantageous if the nanoparticles are tailored for therapy guidance with well-established tomographic imaging techniques such as MRI, CT, or PET/SPECT.^[2,4,19–22] For instance, we recently showed that Fe-B NPs combine the radiosensitization ability for boron neutron capture therapy (BNCT) with MRI and interesting magnetic properties for magnetophoretic accumulation in tissues and magnetic hyperthermia.^[23] BNCT relies upon the accumulation of a ¹⁰B-rich carrier in the cancer tissues to achieve an advantageous therapeutic index, that is, the ratio of effectiveness to side effects on normal tissues, under irradiation with a low-

energy neutron beam.^[20,24] BNCT is increasingly gaining attention as an effective approach for the treatment of cancers with negative prognosis such as melanomas,^[24,25] gliomas,^[26] head and neck tumors,^[27] liver cancer^[28] and lung malignancies as pleural mesothelioma, cancer caused by asbestos fibers.^[29]

Imaging-guided radiotherapy is crucial for BNCT.^[20,22,24,30] The evaluation of ¹⁰B accumulation in the tissues is required for the determination of the appropriate neutron fluence for therapy.^[31–33] This is often performed just from blood analysis and extrapolation to the tumor concentration on the basis of models with large uncertainty.^[20,24,31] The most advanced approaches exploit a tiny fraction of sensitizers labeled with radioactive isotopes (¹⁸F or ¹¹C) and positron emission tomography,^[34–37] but this is expensive and time-consuming, it is not simultaneous to therapy because performed days before neutron irradiation, and the patient is exposed to the β^+ radiations of radioisotopes spread in the whole body and not just in the tumor.^[37] Overall, the clinical procedures for evaluation of the boron uptake and the required neutron fluence are affected by significant uncertainties, which lead to high variability in the clinical outcome of BNCT even within the same clinical trial.^[20,24,34–37]

To date, there are still very few studies on radiosensitizers for combined therapy with more than one radiation type as X-rays and neutrons,^[33,37,38] leaving the potential benefits of radiosensitizers for combined treatment of cancer still far to be understood. XRT is used in more than 50 % of cancer treatments, especially for treating primary non-metastasized solid tumors.^[19,39] Nothing is known about the radiobiological effects of combined radiotherapy with a combined radiosensitizer for XRT and BNCT, which have different depth dose profiles^[40] and penetration depth of emitted particles (hundreds of nm for Auger and Compton electrons from XRT versus microns for alpha particles from BNCT).^[4,41]

Besides, BNCT is promising for the treatment of hypoxic tumor regions because the alpha particles have high linear energy transfer (LET) and induce direct damage in DNA, causing irreparable double-strand breaks, whereas the low-LET particles produced by XRT induce mostly reparable DNA single-strand breaks by indirect damage through generation of reactive oxygen species (ROS), resulting more effective on non-hypoxic tumor regions.^[4,19,20,24,25,42–44] Thus, an open point concerns the treatment of different regions of the body with the most suited radiation type, after administering a combined sensitizer to the patient. For instance, the possibility to expand the dose-response therapeutic window, minimizing the side effects on healthy tissues, as well as the immunological aspects and the opportunity of stimulating and reinforcing immunotherapy, are all unknown.^[25,42]

The described scenario indicates that is of utmost importance developing combined radiosensitizers, compatible with imaging-guided treatments, which can be used as the starting point for advancing the knowledge about combined radiotherapy.

Here we have developed boron-doped gold NPs (Au-B NPs) as nanosensitizers for combined XRT and BNCT aided by CT imaging. Noble metals are used in alloy nanoparticles to achieve efficient sensitization for external radiation sources and chemical stability.^[19,39] Especially Au-based NPs have been intensely studied for their ability to improve the locally delivered dose of radiation in XRT.^[19,39] CT is also widely used for obtaining

S. Bortolussi
Department of Physics
University of Pavia
Pavia 27100, Italy

R. Vago
Division of Experimental Oncology
Urological Research Institute
IRCCS San Raffaele Scientific Institute
Milan 20132, Italy

A. E. Spinelli
Experimental Imaging Center
IRCCS San Raffaele Scientific Institute
Milan 20132, Italy

M. Bekić
Department for Immunology and Immunoparasitology
Institute for the Application of Nuclear Energy
INEP
University of Belgrade
Belgrade 11080, Serbia

M. Čolić
Serbian Academy of Sciences and Arts
Belgrade 11000, Serbia

M. Čolić
Medical Faculty Foča
University of East Sarajevo
Republika Srpska, Foča 73300, Bosnia and Herzegovina

cross-sectional and 3D images by exploiting differential X-ray attenuation and tissue thickness, especially due to the higher speed compared to MRI.^[45] Since the gold atoms in the Au-B NPs provide an effective X-ray absorption, proportional to their concentration, the change of the CT signal, measured in Hounsfield Units (HU), in tissue provides a piece of quantitative information on NPs concentration.^[45,46] Noticeably, CT is the starting point for all the BNCT treatment planning systems.^[20,22,24,30,33] However, CT is not used for evaluation of ¹⁰B content in tissues, because ¹⁰B carriers are not effective X-ray absorbers. Another advantage of Au-B NPs is that the chemistry of surface gold atoms is the most appreciated for the easy and effective bioconjugation of NPs with thiolated molecules like biocompatible hydrophilic polymers, proteins, and peptides.

Indeed, not all elements from the periodic table form alloys, and especially the Au-B phase diagram show complete immiscibility in the solid state in the whole composition range.^[47] To solve this problem, we used a one-step synthetic approach based on laser ablation in liquid (LAL) which proved to be powerful for the achievement of alloy NPs, also when the thermodynamics is unfavorable to alloy formation and there is a great difference in chemical reactivity and oxidation potential.^[48–50] Besides, LAL requires limited manual intervention,^[48–50] is cost-effective,^[51] amenable to scale-up with full automation,^[52] and does not need undesired chemical contaminants or pollutant compounds, because the process starts only from the bulk metal components and the pure solvent.^[53]

Due to the set of favorable features as radiosensitizers for combined XRT and BNCT with therapy guidance by CT imaging, and to the efficient LAL synthetic procedure, the Au-B NPs offer now the possibility to advance the knowledge about combined radiotherapy and its possible benefits in terms of personalized cancer treatments and the improvement of the therapeutic window, which ultimately means the increase of patients' survival rate.

2. Results

2.1. Synthesis and Characterization

The Au-B NPs were obtained using a protocol optimized for the synthesis of gold-based alloy NPs by laser ablation in liquid (Figure 1A).^[13,54,55] A metallic Au-B bulk target was immersed in pure ethanol and ablated with 1064 nm (6 ns, 50 Hz) laser pulses to generate a colloid of Au-B NPs. After LAL, hydrophilic polymers such as dextran (DEX, 10 000 Da) or thiolated polyethylene glycol (PEG, either 5000 or 350 Da) were added to the colloid and, after overnight incubation, the NPs were washed repeatedly with double-distilled water and finally resuspended in pure water. The addition of thiolated PEG after LAL was preferred to the addition in situ during the laser synthesis to avoid the use of a large excess of polymer which should be wasted in the subsequent cleaning steps. In fact, thiols strongly interact with noble metal NPs during the laser synthesis, producing a size-quenching effect that is dependent on the concentration of free thiolated molecules in

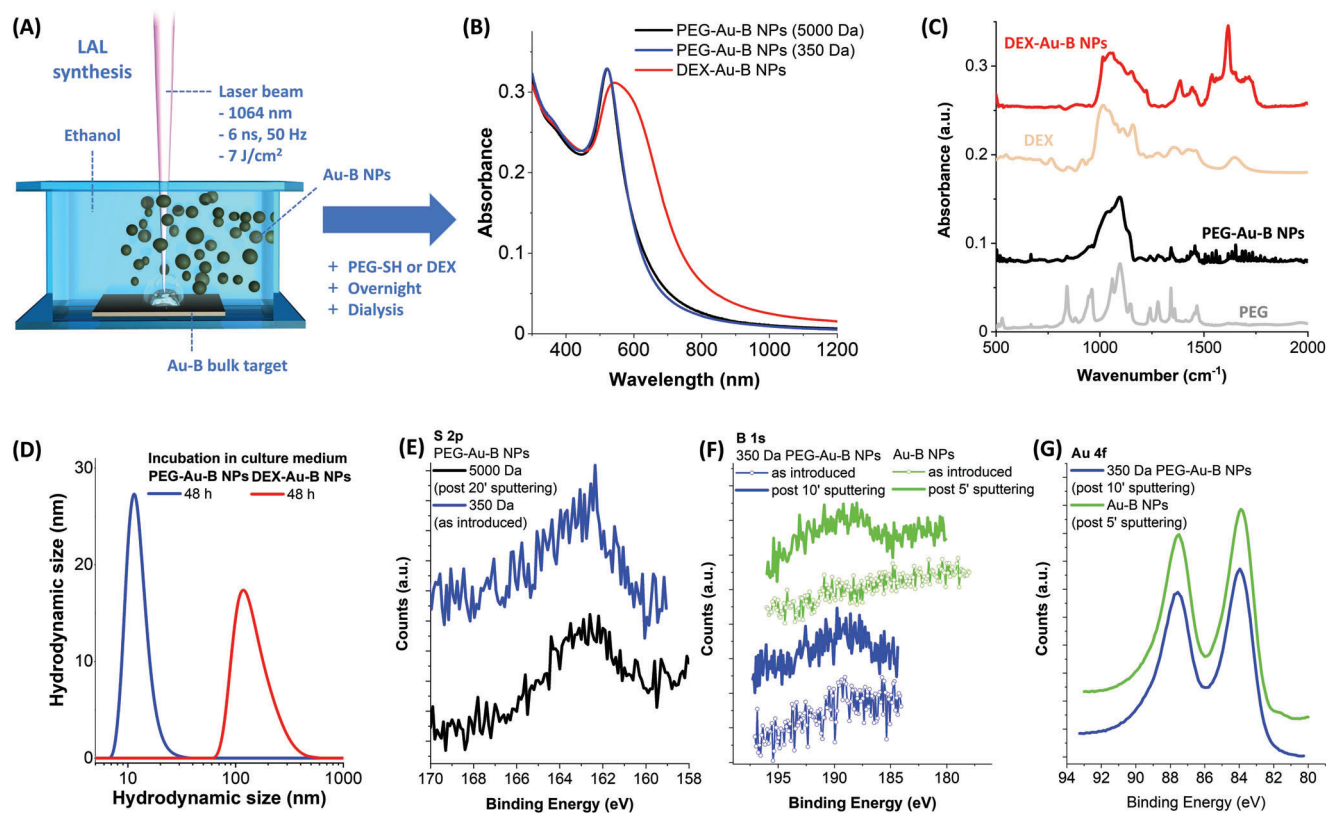


Figure 1. A) Sketch of laser synthesis in liquid of Au-B NPs. B) UV-vis spectra of final Au-B NPs. C) FTIR analysis of dried Au-B NPs samples. D) DLS analysis on Au-B NPs aged for 48 h in cell culture medium. E–G) XPS analysis of S 2p, B 1s, and Au 4f peaks in Au-B NPs samples.

the solution. If the concentration of free thiols changes during the LAL because of the coating of laser-generated NPs, the synthesis results in particles with a heterogeneous or bimodal size distribution.^[48–50,53] Hence, to have a homogeneous size distribution over time, either no thiols or a large excess of thiols should be used, but in the latter case, the large excess of ligands should be removed in the subsequent cleaning steps.

UV–vis spectroscopy (Figure 1B) reveals the presence of the surface plasmon resonance (SPR) band typical of gold nanoparticles, centered at 520 nm for the PEG-Au-B NPs and 535 nm for the DEX-Au-B NPs. When PEG is used, the sharpness and peak position of the plasmon band are indicative of the spherical shape and optimal dispersion of the Au-B NPs. The spherical shape has the highest volume/surface ratio and this is desirable in gold nanoalloys containing easily oxidizable elements like B, because it allows the maximum protection of the less noble element inside the NP.^[13] Besides, the spherical shape allows the most homogeneous coating with polymer chains, ensuring maximum efficacy also in the case of short-chain ligands like the 350 Da PEG.^[56]

Noticeably, the optical properties do not change also using the short-chain PEG. Although the optical properties of the PEG-Au-B NPs with the two PEG lengths are identical, the 5000 Da PEG has been used for the effective coating of a series of Au alloys generated by LAL,^[12,13,15,23,54,55,57–60] thus this coating represents the standard for the comparison of optical properties and other structural characterizations. On the other hand, the 350 Da PEG is shorter, and this is typically associated with a better internalization in cells,^[1–3] as desirable for a radiosensitizer.

Instead, the absorption band of the DEX-Au-B NPs is broader and the plasmon band is red-shifted compared to the PEG-coated NPs, which is indicative of clustered particles.^[61] These results agree with the Fourier transformed infrared (FTIR) spectroscopy, which confirmed the presence of PEG in the PEG-Au-B NPs sample as well as of dextran in the DEX-Au-B (Figure 1C). The FTIR spectrum of PEG has the vibrational fingerprint of the C–O–C stretching at 1100 cm⁻¹ as well as all the distinctive vibrational feature in the 800–1500 cm⁻¹ range.^[15] The spectrum of DEX is dominated by the C–O vibrations at 1000–1150 cm⁻¹ and the O–H stretching at 1650 cm⁻¹, in addition to the stretching and scissoring of C–H groups at 1350–1450 cm⁻¹.^[62]

Since the UV–vis spectroscopy indicates that the polymer-coated Au-B NPs are stable in water, dynamic light scattering (DLS) was used to measure their hydrodynamic size in a cell culture medium (Figure 1D), which is representative of the liquid environment of interest for biomedical applications. Results confirm the stability of PEG-Au-B NPs (350 Da), which have a hydrodynamic size of 12 ± 3 nm after 48 h, while the DEX-Au-B NPs have a larger hydrodynamic size of 150 ± 61 nm. This suggests that the dextran coating cannot avoid the formation of aggregates of NPs because polymer chains are not firmly bound on the surface of the particles. Grafting DEX with thiols through a dedicated chemical procedure would likely bring a functionalized polymer with similar coating efficiency as thiolated PEG,^[63] which however is already commercially available. In fact, the small size and colloidal stability of the PEG-Au-B NPs are explained by the formation of chemical bonds between the sulfur atoms of the thiolated PEG and the gold atoms at the NPs surface. This is a clear indication that the Au-B NPs retain the ease of surface function-

alization and bioconjugation of the pure gold NPs with thiolated molecules. X-ray photoelectron spectroscopy (XPS) further confirmed the presence of sulfur at the surface of 5000 Da PEG-Au-B NPs (Figure 1E), because the S 2p signal becomes well detectable once the external organic PEG shell around the metal particles is etched by 20' of Ar⁺ ion sputtering. Besides, when Au-B-NPs are coated with the short-chained thiolated PEG (350 Da), the S 2p signal is well visible without sputtering (Figure 1E) and the binding energy profile is typical of thiols absorbed on a gold surface.^[64] In the 350 Da PEG-Au-B NPs case, the Au 4f, as well as the B 1s peaks, are both detected after 10' of Ar⁺ ion sputtering (Figure 1F,G), despite the very low photoemission cross section of boron. The presence of Au and B is confirmed further in uncoated Au-B NPs after 5' Ar⁺ sputtering (Figure 1F,G). Noteworthy, the B signal is not clearly detected before the sputtering of the 350 Da PEG-Au-B NPs and the uncoated NPs, which is an indication that boron is bound to the NPs core and not dispersed in the solution. The binding energies of the Au 4f peaks are typical of metallic gold,^[59] while the 1s peak of B spans the 187–193 eV interval, which includes metallic boron as well as boron oxides and suboxides.^[65,66] Considering the low photoemission cross section of boron, this signal is collected from the topmost layer of the NPs surface (a few nm). Hence, this is an indication that boron at the particle surface undergoes oxidation as previously observed in alloys of Au and Ag with transition elements obtained by the same LAL protocol.^[58,59]

The coexistence of gold and boron in the Au-B NPs was confirmed on a sample dried on a silicon substrate and analyzed with energy dispersive spectroscopy (EDS) in an environmental scanning electron microscope (ESEM), which does not require the coating of the sample with a conductive thin film of carbon or gold. Besides the peaks of C (K α) and O (K α) from the organic coating, and the Au M-line, also the B K α line at 0.183 keV is evident in 5000 Da PEG and DEX coated NPs (Figure 2A), while it is not detected in a reference of pure Au NPs coated with PEG and obtained through the same synthetic procedure.

To push the compositional information at the single NP level, the EDS analysis was performed also with a transmission electron microscope (TEM) obtaining the EDS bidimensional maps of Au, B, O, and C in 5000 Da PEG-Au-B NPs (Figure 2B). According to EDS maps, oxygen, and carbon are found in a larger area around the NP, compatible with the presence of a PEG shell. The signal from boron characteristic X-rays is weak compared to the noise background in our EDS experimental conditions, as found also with Fe-B NPs in a previous study,^[23] hence we used electron energy loss spectroscopy (EELS) that is more sensitive to light elements. Again, the boron edge at the characteristic energy of 188 eV^[67] was found in all the EELS spectra collected on four distinct Au-B NPs, while it was not detected in the background spectrum collected in the region between NPs (Figure 2C).

The high-resolution TEM shows that Au-B NPs are polycrystalline and have plenty of defects and dislocations (Figure 2D), which is in accordance with the width of diffraction spots in the selected area electron diffraction (SAED) pattern (Figure 2E). Both techniques indicate that the Au-B NPs have the same face-centered cubic (FCC) crystal structure and lattice spacings of pure gold. That the structure of gold in the Au-B NPs is equivalent to pure Au is confirmed also by the X-ray absorption near edge structure (XANES) spectrum. The Au LIII-edge XANES

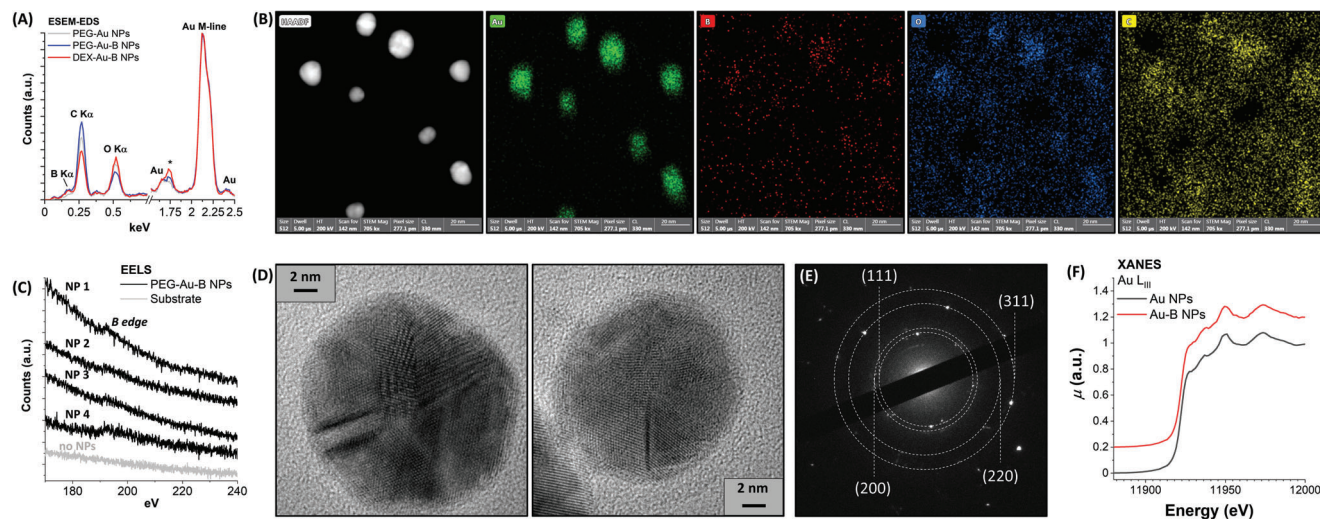


Figure 2. A) ESEM-EDX analysis of Au-B NPs. B) STEM-EDX analysis of 5000 Da PEG-Au-B NPs. C) EELS analysis on different 5000 Da PEG-Au-B NPs and on the TEM grid background between them. D) HRTEM of 5000 Da PEG-Au-B NPs. E) SAED on a group of 5000 Da PEG-Au-B NPs. F) Au L_{III}-edge normalized XANES spectra of 5000 Da Au-B and Au NPs. The Au-B spectrum is shifted along the y-axis for the sake of better visualization.

spectrum of the Au-B NPs shows the same features as the spectrum of Au NPs (Figure 2F). In particular, both samples have the same shoulder at 11 928 eV, which is due to dipole-allowed Au 2p→5d transitions and can be used to monitor the occupancy of the Au 5d states.^[68] Hence, the occupancy of Au 5d states and the electronic structure as projected onto the Au 5d states are also the same. The features at higher energies are of structural origin and are also equivalent for both samples. This is further confirmed by the extended X-ray absorption fine structure (EXAFS) parts of the spectra (Figure S1, Supporting Information), which is a probe for the radial distribution function around the photoabsorbing element and is equivalent for both samples above the unavoidable noise level.

This agrees with the fact that the optical properties of the PEG-Au-B NPs are similar to those of PEG-Au NPs obtained with the same synthetic procedure and in similar size intervals (Figure 3A,B). In this experiment, the PEG-Au-B NPs were fractionated in size by a sedimentation bases separation (SBS) protocol,^[69] to collect size ranges of 5.6 ± 1.7 nm (a), 7.3 ± 2.0 nm (b), 13 ± 5 nm (c) and 19 ± 6 nm (d), as shown in the TEM images reported in Figure 3A. Nonetheless, the PEG-Au-B NPs have lower absorbance at the SPR band maximum than the reference PEG-Au NPs (Figure 3B,C), and the full width at half maximum (FWHM) of the SPR is larger in PEG-Au-B NPs (Figure 3D). Given the small difference in absorbance at the SPR band maximum and FWHM, the experiment was repeated on different batches of Au-B and Au NPs to confirm further the results and the repeatability of the procedure (Figure S2, Supporting Information). Also, we performed several calculations with the Mie model^[57,59] to demonstrate the negligible contribution of small NPs in the samples obtained by the SBS procedure (Figure S3, Supporting Information).

The SPR of gold NPs is known to undergo such slight changes as a consequence of structural disorder, whereas alloying with other elements induces a strong modification of the SPR when the other elements are present as substitutional dopants in the FCC lattice.^[57,70] Hence, these and the overall structural data sug-

gest that B is included as a point defect or is present in disordered regions inside a “matrix” of Au, as previously observed for alloy NPs of immiscible elements like Ag and Fe or Co obtained by LAL, which also exhibited a similar change of SPR.^[15,58,71]

Finally, the composition of the Au-B NPs was quantified with inductively coupled plasma-assisted mass spectroscopy (ICP-MS) analysis, obtaining 88 ± 2 at.% for Au and 12 ± 2 at.% for B in the PEG-Au-B sample, and 89 ± 2 at.% for Au and 11 ± 2 at.% for B in the DEX-Au-B sample. The composition of the PEG-Au-B NPs was investigated also as a function of particle size in the samples obtained with the SBS protocol and in all fractions, the at.% of Au and B are comparable within the experimental error to the unsorted PEG-Au-B sample (Figure 3E). Since the percentage of B does not increase in small Au-B NPs, which have the largest surface-to-mass ratio, this is another indication that boron is embedded in the NPs instead of being segregated at the particle surface. From the TEM-measured average NP size, the estimated number of ¹⁰B atoms for single NP is as high as 10^2 – 4×10^3 (Figure 3F), that is, orders of magnitude larger than in boronophenylalanine (BPA) and carborane derivatives like sodium borocaptate, which are the most used molecular drugs for BNCT,^[20,24,30] and also have problems of solubility without appropriate functionalization or complexation.^[24,72] Noteworthy, the number of ¹⁰B atoms per single Au-B NPs can be further increased fivefold by performing the LAL synthetic protocol with a ¹⁰B-enriched metal target, leading to 5×10^2 – 2×10^4 sensitizers per single NP.

2.2. In Vitro Biocompatibility

In vitro, biocompatibility studies were performed to obtain experimental information on the suitability of Au-B NPs for bio-applications. Since cytotoxicity and uptake of NPs may be dependent on the cell type,^[73–75] cell viability was evaluated by incubating the 350 Da PEG-Au-B and DEX-Au-B NPs with two primary cell types, that is, mouse fibroblasts (L929) and human peripheral

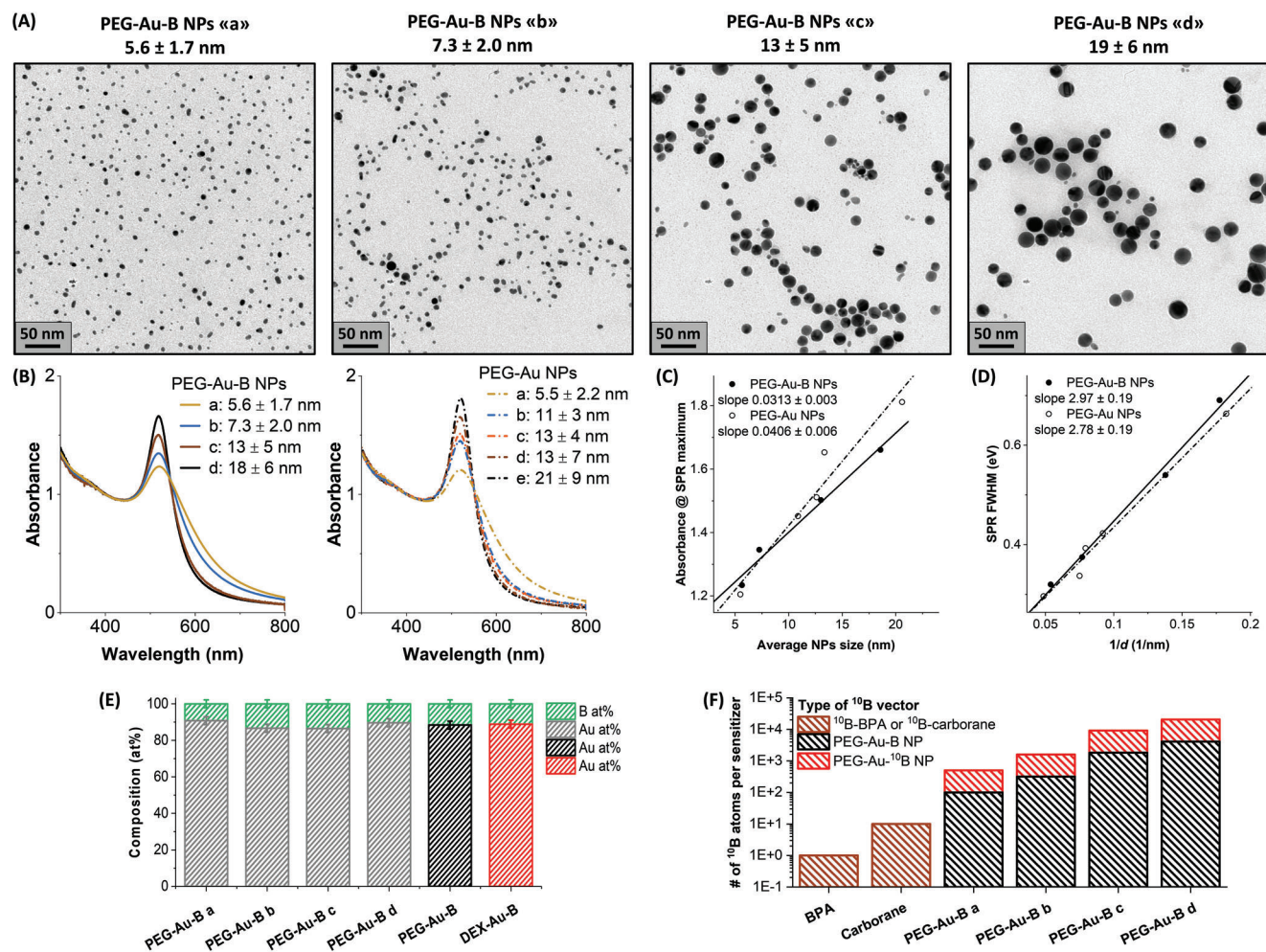


Figure 3. A) TEM of size-selected 5000 Da PEG-Au-B NPs. B) UV-vis spectra of the size-selected 5000 Da PEG-Au-B NPs and equivalent Au NPs. All spectra were normalized at 450 nm for the sake of comparison. C) Absorbance at SPR maximum in the same samples. D) FWHM of the SPR in the same samples. E) Au-B relative composition of the size-selected 5000 Da PEG-Au-B NPs, of the pristine PEG-Au-B sample and of the DEX-Au-B sample. F) Estimated number of ^{10}B atoms for single NP in the size-selected 5000 Da PEG-Au-B NPs and comparison with boron carriers used in clinics.

blood mononuclear cells (PBMC), and two tumor cell lines, that is, mouse melanoma (B16) and human melanoma (A375). All cytotoxicity endpoints (viability, metabolic activity, internalization, necrosis, and apoptosis), except the formation of reactive oxygen species (ROS), were measured after 48 h of incubation at doses of NPs from 0 up to $100 \mu\text{g mL}^{-1}$.

According to the cell viability assay (Figure 4A), the PEG-Au-B NPs are well tolerated by the four cell types even at the highest concentration, which was associated with survival $>75\%$ after 48 h. The DEX-Au-B NPs have a similar effect but slightly lower cell vitality at the two highest concentrations (75 and $100 \mu\text{g mL}^{-1}$), compared to PEG-Au-B NPs, especially in tumor cell lines and human PBMC (Figure 4B). The low cytotoxicity at higher concentrations was confirmed by the measure of the metabolic activity of cells (MTT assay) in the presence of the two types of Au-B NPs (Figure 4C). The internalization of Au-B NPs showed a dependence of the uptake on the polymeric coating, which also means a difference in hydrodynamic size and colloidal stability, and on the cell type (Figure 4D). In fact, the highest internalization index was measured for DEX-Au-B NPs by the hu-

man Mo/M ϕ phagocytes from PBMC cultures, whereas the internalization of PEG-Au-B NPs by L929 and B16 cells was the lowest. No internalization of both types of NPs by lymphocytes from PBMC cultures was observed. Overall, the observed uptake confirms that NPs are in the size range for crossing the cell plasma membrane by passive transport,^[2,72] in agreement with DLS analysis.

A more quantitative estimation of NPs uptake was performed by ICP-MS on cells incubated at $20 \mu\text{g mL}^{-1}$ of Au-B NPs for 24 h. The results confirmed the semiquantitative evaluation for the various cell types (Figure S4, Supporting Information) and quantified the accumulation of PEG-Au-B NPs in the range of pg of Au per single cell. In the case of DEX-Au-B NPs, the amount of Au per cell is typically one order of magnitude higher than with the PEG coating. Noteworthy, even in the sample with the largest accumulation of Au-B NPs the ICP-MS procedure has a boron limit of detection (LOD) 1 order or magnitude higher than what would be required to measure its content inside cells, due to the complex cell culture biological matrix. Conversely, the LOD for a high-Z element like Au is 2 orders of magnitude lower than

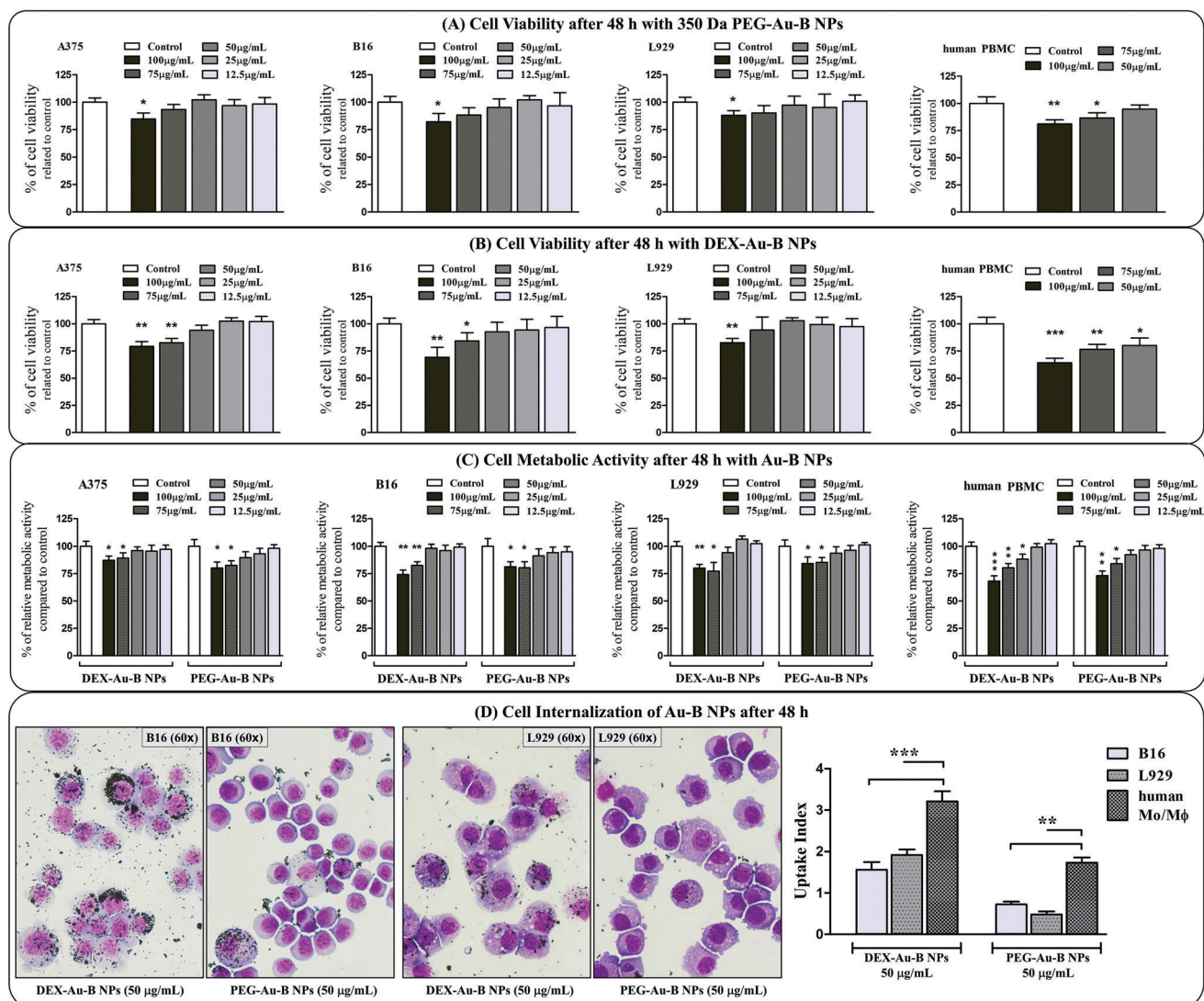


Figure 4. A) Cell viability after 48 h incubation with 350 Da PEG-Au-B NPs, determined by Trypan blue staining. B) Cell viability after 48 h incubation of four cell lines with DEX-Au-B NPs. The results in (A) and (B) were presented as relative values (%), compared to controls used as 100%. C) Cell metabolic activity after 48 h incubation with 350 Da PEG-Au-B or DEX-Au-B NPs, determined by the MTT test. The optical density (OD) of the dissolved formazan in control cultures was used as 100% values. The metabolic activity of cultures with NPs was presented in % relative to controls. D) Cell internalization after 48 h incubation with 350 Da PEG-Au-B or DEX-Au-B NPs. Left: representative images of cytopins showing the internalized NPs at a concentration of 50 µg mL⁻¹. Original magnifications x 40. Right: uptake index of NPs internalization. All values are given as mean values ± SD of four independent experiments. **p* < 0.05; ***p* < 0.01; ****p* < 0.005 compared to corresponding controls (A–C) or cell lines (D) (two-way ANOVA with Tukey's multiple comparisons test).

for B, evidencing the advantage of the alloy NPs for the indirect quantification of boron in cells through ICP-MS.

The limited cytotoxicity observed in the vitality and MTT assays at the highest NPs dose was prevalently associated with late apoptosis events in L929 and human PBMC, while both early and late apoptosis was detected in B16 cells (Figure S5, Supporting Information). Instead, there was no evidence of the increase in necrosis compared to the control. We found a correlation between the higher rate of apoptosis in cells incubated with DEX-Au-B NPs and the evidence of ROS production (Figure S6, Supporting Information), which was expected considering the larger uptake index compared to the PEG-Au-B NPs. These re-

sults suggest that the coexistence of boron and gold at the nanoscale may be associated with higher cytotoxicity than PEG-coated pure Au NPs, which were not-cytotoxic up to concentrations of 100 µg mL⁻¹,^[75] and pure B NPs also evidenced limited cytotoxicity up to 250 µg mL⁻¹.^[76]

2.3. Theranostic Potential

Motivated by the abundance of boron atoms per NP, the generation of charged particles with high LET upon the capture of thermal neutrons was assessed by neutron autoradiography.

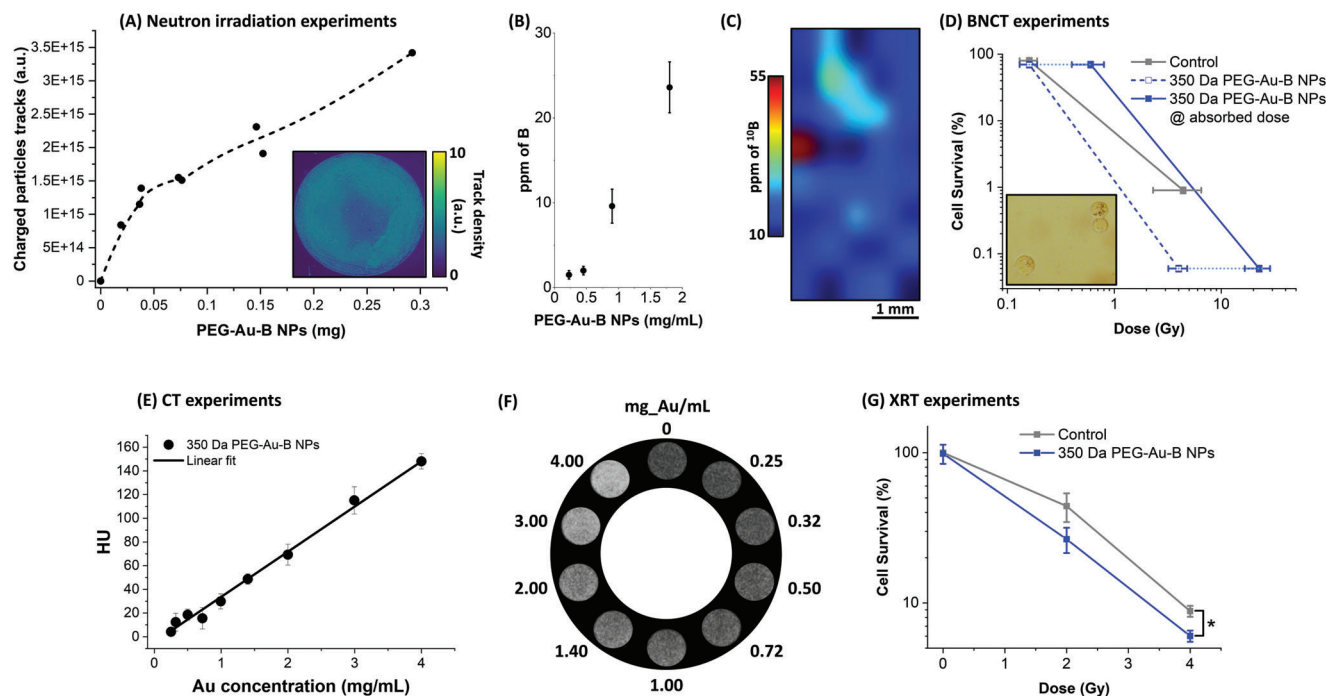


Figure 5. A) Correlation between charged particle tracks and the mass of PEG-Au-B NPs deposited on CR39 films. Inset shows a qualitative bidimensional map of charged particles tracks intensity. B) Assessment of linearity in boron concentration versus PEG-Au-B NPs concentration in aqueous solution. C) Bidimensional neutron autoradiography map of ^{10}B distribution in UMR-106 cells treated with the PEG-Au-B NPs. D) Cell survival experiments performed at 10 and 250 kW of neutron irradiation power for 10' in UMR-106 cells treated with the PEG-Au-B NPs. Inset: optical microscopy image of cells before the irradiation experiment. E) Plot of HU versus Au concentration collected on phantoms containing the 350 Da PEG-Au-B NPs at variable dilution. CT images of phantoms' cross-sections are also reported in (F). G) Cell survival experiments at 0, 2, and 4 Gy in PC3 cells treated with the PEG-Au-B NPs (* corresponds to $p < 0.05$, One-way ANOVA). All data are shown in terms of means \pm SE ($N = 3$). Results for in vitro experiments are relative to the respective sham-irradiated controls.

Initially, drops of 350 Da PEG-Au-B NPs were deposited and dried at room temperature on a high LET-sensitive film (CR39) functioning as a solid-state charged particle track detector.^[77] The CR39 slides can register the tracks of charged particles (α and Li^+) generated by the ^{10}B atoms in Au-B NPs, as shown in the qualitative bidimensional map of Figure 5A obtained after irradiation in the thermal column of a TRIGA Mark II reactor with a thermal neutron fluence of $(9.8 \pm 0.5) \times 10^{12} \text{ cm}^{-2}$. The results show the expected increase of charged particle tracks with the amount of NPs drop cast on the CR39 film (Figure 5A), with a saturation when NPs loading exceeded the linearity interval due to packing of the particles in the deposit. To avoid this problem, the quantitative assessment of linearity in boron concentration versus NPs concentration was obtained by neutron autoradiography of aqueous solutions of PEG-Au-B NPs faced to CR39 slides with a thermal neutron fluence of $2.0 \pm 0.1 \times 10^{10} \text{ cm}^{-2}$, upon calibration of the generated charged particles with a ^{10}B standard solution of BPA (Figure 5B).

Since boron is present with high abundance in the Au-B NPs, their potential for BNCT was tested in vitro in a rat osteosarcoma cell line (UMR-106). UMR-106 cells were selected because the effect of neutron irradiation is well characterized in this cell line, both in the absence of boron and in the presence of the clinically used boron carrier BPA,^[78,79] thus representing a good benchmark for in vitro BNCT experiments. Besides, UMR-106 cells quickly grow and reach confluence, which is useful for BNCT

experiments needing a large number of cells to measure boron uptake by neutron autoradiography.^[78,79]

The cells were treated for 18 h with 0.76 mg ml^{-1} of 350 Da PEG-Au-B NPs. The 350 Da PEG-Au-B NPs were selected for the smaller hydrodynamic size and colloidal stability as well as for the slightly better in vitro biocompatibility, also evidenced by a lower tendency to agglomeration compared to DEX-Au-B NPs. First, the boron uptake was evaluated by neutron autoradiography, indicating that the content of ^{10}B in cell cultures reached 24 \pm 7 ppm versus a background of 0.7 ± 0.6 ppm in cells untreated with the Au-B NPs. Although the bidimensional neutron autoradiography maps indicate a low uniformity of NPs distribution in the cell culture, ranging from 10 to 50 ppm of ^{10}B (see Figure 5C), these values correspond to a total boron uptake of 250–50 ppm, which is a remarkable value for untargeted NPs and fall in the therapeutic window.^[24,72]

Then, the cell survival experiments were performed at 10 and 250 kW of irradiation power for 10' in UMR-106 cells treated with the PEG-Au-B NPs and without NPs (control). The results evidenced a considerably low survival of cells treated with the NPs (0.060 ± 0.006 % at the highest irradiation power, Figure 5D). The dose absorbed by cells was evaluated in detail by means of Monte Carlo calculation considering all the charged secondary radiation produced by neutron irradiation,^[78] resulting in a much higher value for samples treated with Au-B NPs (0.6 ± 0.2 Gy and 23 ± 6 Gy) than for the control (0.16 ± 0.03 Gy and 4.4 ± 2.1 Gy).

The survival curve of Au-B NPs treated cells compares well with the positive control represented by BPA-treated cells (Figure S7, Supporting Information). Although the BPA curve is steeper, it should be noted that BPA enters cells via an active mechanism mediated by the LAT-1 expression,^[80,81] whereas polymer-coated NPs mostly enter cells by phagocytosis and a fraction of NPs may accumulate on cell membrane.^[1–3] This has an effect on the efficiency of DNA damage, which depends on the proximity of the boron to the cell nucleus during irradiation.^[20,22,25,30] On the other hand, cells were incubated with BPA at a 10B concentration which was 90 times higher (18 times higher total B concentration) than in the NPs experiment, indicating that Au-B NPs efficiently act as intracellular boron carriers. One can hypothesize that the survival of cells treated with Au-B NPs could be much lower at parity of absorbed dose if the NPs had entered the cells instead of remaining attached to the cell membrane, as suggested by the comparison with the BPA curve and by optical microscopy (see inset of Figure 5D) because boron that is located outside the cells is less effective in causing lethal damage to the DNA.^[20,24]

Taking advantage of the Au scaffold of these NPs, CT contrast ability and signal linearity versus NPs concentration was assessed (Figure 5E). CT is based on the absorption of X-rays with energy in the 30–120 keV range^[82] and Au atoms ($Z = 79$) have an X-ray linear attenuation coefficient ≈ 300 times larger than a low- Z element like B ($Z = 5$).^[83] Therefore, the distribution of Au-B NPs can be monitored with CT and evaluated quantitatively thanks to the linear dependence of X-ray attenuation signal on the concentration of Au atoms, as demonstrated by the plot of Figure 5E and qualitatively by the tomographic images of phantoms containing the NPs at increasing concentration in Figure 5F. The slope of the X-ray attenuation versus NPs concentration is 38 ± 1 HU (Hounsfield Units) mL mg^{-1} , which is the value expected for Au NPs in the standard experimental conditions adopted (X-ray tube operating at 80 kV), and is higher than the literature values for the commercially available iopromide (16 HU mL mg^{-1}) exploited in clinics.^[84,85]

Furthermore, the effective absorption of X-rays by Au-B NPs is exploitable for X-ray radiosensitization under irradiation conditions proper of XRT, that is, at therapeutic photon doses.^[19,39] XRT sensitization by high- Z elements like Au exploits the emission of photoelectrons, Compton electrons, and Auger electrons after absorption of an X-ray photon, and these types of ionizing radiation can induce cell apoptosis and necrosis by direct damage of DNA or, more frequently, by interaction with water to produce ROS, which is much more easily generated in presence of oxygen.^[19,39,44,86] Hence, the XRT potential was tested in vitro in a typical cancer cell model (PC3, human bone metastasis of grade IV prostatic adenocarcinoma). PC3 cells are selected because they are well-known and intensively used for in vitro XRT studies, both in the absence of sensitizers and in the presence of Au NPs or other nano-sensitizers (see Table S1, Supporting Information), thus representing a suitable benchmark for in vitro XRT experiments. The cells were treated for 24 h with $50 \mu\text{g Au mL}^{-1}$ of 350 Da PEG-Au-B NPs. Then, the cell survival experiments were performed after 0, 2, and 4 Gy of X-ray irradiation dose. The results confirmed the superior ability of Au-B NPs to act as sensitizers, resulting in a statistically significant difference in survival at 4 Gy, that is, 0.060 ± 0.008 in cells treated with the NPs versus 0.088 ± 0.007 for the control (Figure 5G). Noticeably,

the concentration of NPs was in the standard range for XRT experiments and is 15 times lower than what was required to stay in the boron therapeutic window for the BNCT experiment.

3. DFT Modelling and Discussion

The development of innovative multifunctional theranostic vectors is crucial for expanding the range of cancer therapeutic approaches. A still scarcely investigated field consists of the combination of BNCT and XRT, supported by CT imaging for the localization and quantification of radiosensitizers. Nanotechnology can provide the tools for addressing this endeavor, but the large-scale realization of this type of nanomedicine is still challenging, especially when considering reproducibility, environmental sustainability, and cost affordability of the process.

To address this challenge, alloy NPs of Au and B have been produced starting from a LAL process. Despite the difficulty of detecting boron in the high Z matrix of Au and the lack of information on the Au-B systems at the nanoscale, the structural analyses revealed the coexistence of the two elements in the Au-B NPs. However, the Au-B NPs maintained a marked Au NPs character, such as the advantageous surface chemistry with thiolated compounds, biocompatibility, and stability.

Although boron is known to have a high tendency to organize in amorphous structures, relatively little is known about its solubility and mobility in the high-packing lattice of metals.^[87,88] Previous studies indicated that boron may accumulate at concentrations as high as 20 at.% in platinum group metals, adopting interstitial impurity sites due to its small atomic radius.^[67,88] Nonetheless, interstitial doping with the boron concentration measured in Au-B NPs (11–12 at.%) is expected to significantly affect the electronic structure and the plasmon properties of the alloy NPs.^[67,88] Instead, the experiments indicate no changes in the electronic structure of Au and minor effects on the SPR, while high defectivity was observed by HRTEM and SAED. As reported previously for LAL synthesis of alloy NPs with immiscible plasmonic (Ag) and non-plasmonic (Fe, Co) elements, point and planar defects can be the site of segregation for the minority element in the scaffold of the plasmonic metal.^[58,71] Besides, XPS indicated that B is present with a range of oxidation states from metallic to suboxides and oxides, suggesting that oxidation may contribute further to element segregation.

To obtain more information on the Au-B system, such as the formation energy (E_{form}) and the change in the cell volume (ΔV), density functional (DFT) calculations were performed on three possible models of alloying: i) substitutional alloys, where each B atom replace an Au atom in the bulk gold lattice and modeled using special quasi-random structures; ii) interstitial alloys, where B atoms sit at interstitial sites in the bulk gold lattice; iii) segregated alloys, where small B clusters are placed in the FCC cell site left by an Au vacancy in the bulk gold lattice. All alloy types are modeled within $2 \times 2 \times 2$ supercells containing 32 FCC sites.

In the substitutional models, the E_{form} per B atom is almost the same when 2 or more Au atoms are replaced with B (Figure 6A). This is accompanied by a continuous lattice contraction, which remains below 2% up to the substitution of 10% of Au atoms with B (Figure 6B). This lattice contraction is relatively small for Au alloys,^[57] and measuring it beyond experimental uncertainty

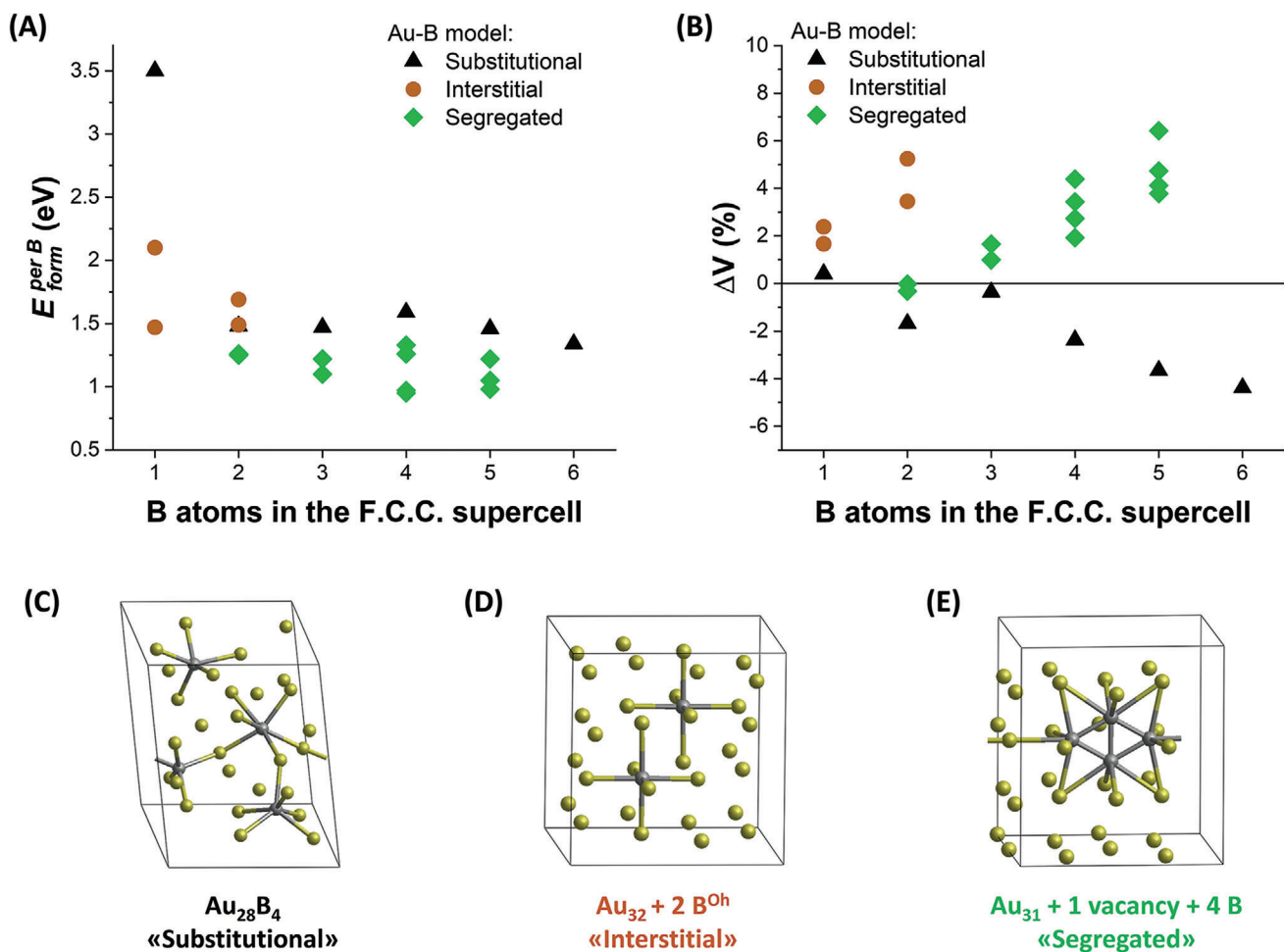


Figure 6. DFT calculations on substitutional, interstitial, and segregated Au-B alloy models. A) E_{form} per B atom (eV). B) Volume variation (%). C–E) Supercells containing 4 B atoms in a substitutional model (C), in an interstitial alloy model with 2 B atoms in O_h sites (D), and in the lowest-energy segregated model, showing the DFT prediction of B atoms clustering inside the Au scaffold (E).

may be challenging in systems with high defectivity as our polycrystalline NPs.

Interstitial alloys can be obtained by inserting a B atom in octahedral (O_h) or tetrahedral (T_d) interstices.^[87] In agreement with Hu et al.^[87] we found that $Au_{32}B^{T_d}$ has a formation energy of 2.10 eV, while the $Au_{32}B^{O_h}$ is more stable and has a formation energy of 1.49 eV (Figure 6A). The formation energy of the $Au_{32}2B^{O_h}$ structure, where 2 O_h sites are occupied by B, remains 1.49 eV per B atom, thus also in this model, there is a very small change of E_{form} per B atom upon increasing the amount of B. Since the formation energy of the substitutional $Au_{30}B_2$ alloy also is 1.48 eV per B atom, very close to the interstitial $Au_{32}2B^{O_h}$ model, there is no net preference for either structure. However, a fairly large variation of the lattice spacing is predicted for interstitial alloys (Figure 6B), so that the volume of the cell increases by 3.5% when just 2 octahedral (O_h) interstices are occupied by B atoms, that is at 6% atomic B.

Concerning the segregated models, a number of possible arrangements were considered ranging from the $Au_{31}B_2$ to the $Au_{31}B_5$ compositions (see Supporting Information for details). As shown in Figure 6A, the E_{form} per B atom are systematically

lower than those of substitutional and interstitial alloys, with a minimum of 0.94 eV for the $Au_{31}B_4$ case (Figure 6A). Hence, such structures are thermodynamically favored over substitutional and interstitial alloys, and in addition have relatively small volume changes compared to pure Au ($\approx 3\%$ for one of the $Au_{31}B_5$ models, Figure 6B).

From the structural point of view, the optimization of substitutional alloys leads to largely distorted structures. For instance, when 3 Au atoms are substituted by B ($\approx 10\%$ of B) the FCC structure is barely distinguishable, and above this threshold, the structures are mostly disordered (see for instance Figure 6C and Supporting Information). Conversely, the interstitial alloys retain the FCC structure (Figure 6D and Supporting Information). Also, the segregated models, in which B atoms are allowed to cluster within the void left by an Au vacancy, retain well-organized lattice structures (Figure 6E and Supporting Information). The tendency toward amorphization of substitutional alloys can be attributed to the predilection of B to be surrounded by a limited number of nearest neighbors (NNs).^[87,88] This requirement is already satisfied in interstitial alloys, where B has 4 NNs at 2.05 Å when at a T_d site and 8 NNs at 2.2 Å when at an O_h site. When B

is in an FCC site, it is surrounded by 12 NNs which are at a much larger distance of 2.9 Å. This situation destabilizes substitutional alloys leading to a remarkable reorganization of the lattice structure, with a change in the coordination sphere of B atoms and ultimately producing disordered structures.

Thus, the insights from the DFT calculations agree with the multiple experimental evidence in suggesting that the Au-B system has an energetic advantage for boron segregation, with respect to dilution as substitutional or interstitial dopants. We know from XPS data that boron in the Au-B NPs is present also with the oxidation state of suboxides and oxides. Hence, given the low oxidation potential of boron, this element was able to react with trace oxygen during the LAL process, further favoring the short-range segregation of B in the Au scaffold. All this led to Au-B NPs with the desired theranostic features for nanomedicine exploitation and further empowering with specific surface functionalities for better cell internalization and cell targeting ability.

4. Conclusion

We developed a new Au-B multifunctional theranostic nanovektor for the combination of BNCT and XRT supported with CT for the localization and quantification of the radiosensitizers in tissues, which is a crucial aspect of BNCT. The Au-B NPs were obtained from laser ablation in a liquid process and subsequently coated with biocompatible polymers such as DEX or thiolated PEG. The laser-assisted synthetic pathway granted reproducibility, environmental sustainability, and cost affordability, as required for the scale-up of the production route. The structural features of Au-B NPs were identified, demonstrating the coexistence of the two elements in the NPs, which is an absolute novelty in the panorama of nanotechnology. DFT calculations and experimental data indicate that the coexistence of the two immiscible elements was possible by B clustering and segregation in the FCC Au lattice. Hence, Au-B NPs have a marked gold character, including the advantageous surface chemistry with thiolated compounds, biocompatibility, and stability, and proved to act as radiosensitizers for both BNCT and XRT, as well as allowing the localization and quantification by CT imaging. A further fivefold enhancement of BNCT performances is straightforward by using a ^{10}B enriched composition. Overall, the Au-B NPs have the optimal features for the investigation of combined BNCT and XRT, supported by CT imaging and with the easy integration of surface agents for cell targeting and internalization, which are crucial for appropriate intracellular localization. By this Au-B nanotheranostic tool, it is now possible to shed light on scarcely investigated or completely new aspects such as the combination of BNCT and XRT, the CT guidance for radiotherapy doses, and the role of radiosensitizers localization in the tissues and cells during the double-radiotherapy treatment, ultimately leading to the expansion of the therapeutic window for several types of cancers with a negative prognosis.

5. Experimental Section

Synthesis: Au-B NPs were obtained by LAL focusing the pulses of a Q-switched Nd: YAG laser (1064 nm, 6 ns, 50Hz) with an f 10 cm lens on an Au-B metal plate (50:50 at%, 99.99% pure, Mateck) placed at the bottom

of a cell containing pure ethanol (HPLC grade, Sigma-Aldrich). The fluence was set to 20 J cm^{-2} and the cell was mounted on a motorized XY scanning stage (Standa) controlled with a 2-axis stepper and a DC motor controller. The colloid was then incubated overnight at room temperature with either 5000 Da (1 mg mL^{-1} , Laysan Bio), 350 Da PEG-SH (0.1 mg mL^{-1} , Sigma-Aldrich) or 10 000 Da DEX (5 mg mL^{-1} , Sigma-Aldrich). After incubation, the Au-B NPs dispersions were washed multiple times with distilled water using dialysis concentration membranes (cut-off 10 000 Da, Sartorius) by centrifugation at 1000 rcf to remove ethanol, unbound polymer, and any other synthesis by-product. Finally, the NPs were resuspended in distilled water and used for following experiments or stored in the freezer.

Reference 5000 Da PEG-coated gold (PEG-Au) NPs were obtained with the same procedure but starting from a bulk Au target (99.99 % pure).

SBS on PEG-Au-B and PEG-Au NPs was performed according to a previously established protocol.^[69] Briefly, the colloids were placed in 1.5 mL tubes and centrifuged at different speeds increasing from 50 to 4000 rcf (1 h for each run), collecting the sediment at each run (which was resuspended in distilled water) and centrifuging the supernatant again at the next higher speed.

Characterization: UV-vis spectra were recorded with a JASCO V770 spectrophotometer using quartz cells with a 2 mm optical path or by an Avantes portable spectrometer (AvaSpec-ULS2048CL-EVO) coupled with a deuterium-halogen lamp (AVA-Light-DHC). DLS was performed with a Malvern Zetasizer Nano ZS in DTS1070 cells. FTIR spectroscopy was performed with a Perkin Elmer 1720X FTIR spectrophotometer, depositing the dried samples on a KBr window.

XPS analysis was performed at room temperature using normal emission geometry with a modified VG ESCALAB MKII (Vacuum generators, Hastings, England) equipped with non-monochromatized Al/Mg twin anode X-ray source (Al anode X-ray source, $K\alpha$ radiation at 1486.6 eV), a sputter gun, a hemispherical electrostatic analyzer with a five-channeltron detector, and setting pass energy of 50 eV for optimal signal-to-noise ratio. The samples were obtained by dropwise deposition of NPs dispersion on a Cu sample holder and drying at room temperature.

Microanalysis was performed with an ESEM model FEI Quanta 200 on Au-B NPs samples drop cast on a crystalline Si substrate, without further metallization. TEM analysis was carried out at 300 kV with a JEOL JEM 3010 microscope using a Gatan Multiscan CCD 794 Camera. For each sample, a drop of the solution was deposited on a copper grid coated with an amorphous carbon film. ImageJ software was used to measure the geometrical (Ferret) size distributions. The average Ferret size and standard deviation were obtained from statistics considering more than $n = 500$ NPs for each sample. STEM-EDS and EELS analysis was performed with a TEM Talos F200S G2 operating at 200 kV and equipped with two windowless silicon drift X-ray detectors and a Gatan Infinium SE/976 spectrometer.

ICP-MS measurements were carried out with an Agilent Technologies 7700x ICP-MS (Agilent Technologies International Japan, Ltd., Tokyo, Japan) equipped with an octupole collision cell operating in kinetic energy discrimination mode, which was used for the removal of polyatomic interferences and argon-based interferences. For instrument calibration, standard Au and B solutions were purchased from Spectrascan, Agilent Technologies, and Inorganic Ventures (CLPP-CAL-1). Samples digestion was performed with aqua regia at 90 °C for 1 h.

Fluorescence XAS data were collected at the BM08 LISA beamline (European Synchrotron Radiation Facility, ESRF, Grenoble, experiment 08-01-1020) at the Au LIII-edge (11 918.7 eV). A Si(111) double crystal monochromator was used; the harmonic rejection was realized by Pd mirrors, having a cut-off energy of 20 keV, and a 13-element Ge fluorescence detector. The energy calibration was performed by measuring the absorption spectrum of metallic Au. For the measurements, the colloidal samples were spotted onto Millipore filters and then cooled down to 80 K, aiming at increasing the EXAFS oscillations. The reproducibility in energy was assured by simultaneously measuring the XAS spectra of an Au foil, and for every scan, was observed to be better than 0.1 eV. For the XANES analysis, the spectra were processed by subtracting the smooth pre-edge background fitted with a straight line and then normalized to unit absorption at ≈ 600 eV above the edge, where the EXAFS oscillations were not visible anymore. The EXAFS extraction was done using the ATHENA code.

Cytocompatibility, ROS Production, and Uptake Studies: Mouse fibroblasts (L929), mouse melanoma (B16), and human malignant melanoma (A375) were obtained from ATCC (Rockwell, MD, USA) and human PBMC from blood volunteers upon signing an informed consent and approval of the study by the Ethical Committee of INEP, Belgrade, Serbia. PBMC were isolated by centrifugation of citrated blood over the Hystopaque gradient. In all assays, the cells were cultured in RPMI 1640 medium, supplemented with 10% FCS (Sigma, Munich, Germany), 2×10^{-3} M l-glutamine (Sigma), 100 U mL^{-1} penicillin, 100 mg mL^{-1} streptomycin (all antibiotics from ICN, Costa Mesa, CA, USA), and 50×10^{-6} M 2-mercaptoethanol (Sigma). The cells were cultured with different concentrations of Au-B NPs from 12.5 to $100 \text{ } \mu\text{g mL}^{-1}$ in 96-well plates (Sarstedt, Numbrecht, Germany), at 10^4 cells per well (each in triplicates), or without NPs (negative control). The cell lines were allowed to adhere overnight at $37 \text{ }^\circ\text{C}$, before the addition of ultrasonically treated NPs.

To evaluate the metabolic activity of cells, after cultivation for 48 h at $37 \text{ }^\circ\text{C}$, $20 \text{ } \mu\text{L}$ of MTT (Sigma) solution (5 mg mL^{-1} in PBS) was added to each well and the plates were incubated for additional 4 h. Wells with an MTT solution without the cells served as blank controls. The formazan crystals were dissolved overnight by the addition of $150 \text{ } \mu\text{L}$ of $0.01 \text{ N HCl}/10\%$ sodium dodecyl sulfate (Merck, Darmstadt, Germany). The next day, the optical density (OD) value was read at 570 nm (ELISA reader, Behring II). The results were presented as the relative metabolic activity compared to the negative control, used as 100%. For the apoptosis/necrosis assay, an annexin-V-fluorescein isothiocyanate (FITC)/propidium iodide (PI) kit (Invitrogen, Carlsbad, CA, USA) was used according to the manufacturer's protocol, followed by flow cytometry analysis (CyFlow Cube 6, Partec GmbH, Munster, Germany). The cell lines were seeded in 24-well plates (Sarstedt) (10^5 cells per well or 3×10^5 cells per well for PBMC) and allowed to adhere at $37 \text{ }^\circ\text{C}$. After 2 h, cells were treated with different concentrations of Au-B NPs or culture medium alone (negative control) for 48 h at $37 \text{ }^\circ\text{C}$. After cultivation, media were removed, and the cell lines were washed three times with PBS and trypsinized. Cells were collected by stronger pipetting. The collected and washed cells were stained and analyzed. The assay enabled the identification of necrotic (annexin-V-FITC-/PI+) cells, living (annexin-V-FITC-/PI-) cells, early apoptotic (annexin-V-FITC+/PI-) cells, and late apoptotic/secondary necrotic (annexin-V-FITC+/PI+) cells.

For the viability assay, the cells were cultured as described above. The Trypan blue dye exclusion test was used to determine the number of viable cells present in a cell suspension. The viability was determined by manual microscopic observation after staining cells with 0.2% Trypan blue solution.

ROS production was detected by staining the cells using dihydrorhodamine (DHR) 123 dye following the manufacturer's protocol (Sigma-Aldrich, St. Louis, MO, USA). The cells were cultivated and proceeded for apoptosis/necrosis assay. After 24 h of cultivation, the cells were incubated with 5×10^{-6} M DHR123 in PBS for an additional 30 min at $37 \text{ }^\circ\text{C}$. Subsequently, after washing in PBS, the fluorescence intensity (fi) was analyzed in an LSRII flow cytometer (Becton Dickinson). For comparison, blank samples with the cells without DHR123 loading (with and without Au-B NPs) were used. Appropriate positive controls were cells treated with 0.3% hydrogen peroxide (H_2O_2) (Sigma-Aldrich). Results were presented as mean fi or percentage of DHR123-positive cells, from three independent experiments.

For uptake experiments, the cells (5×10^4 per well) were seeded onto 13 mm glass coverslips (Sarstedt), placed in 24-well plates (Sarstedt), and incubated in cell culture medium for 2 h at $37 \text{ }^\circ\text{C}$ to adhere. The cells were then incubated with Au-B NPs overnight at $37 \text{ }^\circ\text{C}$. Coverslips were removed from the plates, washed thoroughly in PBS, air-dried, and fixed with methanol (Merck). After fixation and drying, coverslips cells were stained with May Grunwald Giemsa. Air-dried specimens were mounted with Canada balsam (Merck) and analyzed with a light microscope (Nikon Eclipse 5i equipped with a Nikon DXM1200C camera, Tokyo, Japan). Internalization of NPs (black intracellular granules) was checked using a semi-quantitative method as described in the previous article.^[23]

For NPs uptake measured by ICP-MS, 5×10^5 L929, A375, or B16 cells were seeded in 6-well plates and cultivated overnight in a complete culture

medium to adhere. PBMCs (2×10^6) were placed in 24-well format plates. Incubation with Au-B NPs ($20 \text{ } \mu\text{g mL}^{-1}$) was performed in a cell culture medium for the next 24 h. All cultures ran in duplicates. After the incubation period, adherent cell cultures (L929, A375, and B16) were thoroughly washed 3 times with PBS before trypsinization. Plates with non-adherent PBMCs were spun at 1000 rpm for 10 min, followed by careful removal of the supernatant. To improve the removal of non-internalized Au-B NPs, transwell inserts were used (Greiner Bio-One, Austria). Considering the average diameter of the cell populations for L929, A375, and B16 ($5\text{--}10 \text{ } \mu\text{m}$) and for PBMCs ($6\text{--}25 \text{ } \mu\text{m}$), the cells were placed in the upper chamber of transwell inserts with a $3 \text{ } \mu\text{m}$ diameter of a filter pore in 1 mL of PBS, while non-internalized Au-B NPs were washed away through the filter via careful pipetting. The process was repeated at least 5 times. After that, cells were collected, resuspended in 1 mL of PBS, and counted in Trypan blue. ICP-MS analysis was carried out after digestion with aqua regia at $90 \text{ }^\circ\text{C}$ for 1 h.

BNCT Experiments: The neutron capture by ^{10}B atoms was evaluated by neutron autoradiography, according to a well-established procedure.^[77] Briefly, aqueous solutions of Au-B NPs were deposited by serial drop-casting on CR39 solid-state nuclear track detectors and dried at room temperature or placed in the well plate with the liquid faced to a CR39 slide. The CR39 films were irradiated in the thermal column of the TRIGA Mark II reactor operating at 2 kW for 30 min, with a neutron fluence of $(2 \pm 0.1) \times 10^{10} \text{ cm}^{-2}$ for the track counting analysis, while qualitative imaging of the sample the reactor was operated for 2 h at 250 kW , obtaining a neutron fluence of $(9.8 \pm 0.5) \times 10^{12} \text{ cm}^{-2}$. Quantification of the generated charged particles was obtained by etching the CR39 films with PEW40 solution, imaging the tracks generated by the charged particles emitted from the ^{10}B atoms with a LEICA M205 FA stereo microscope, and counting the number of tracks per drop by means of the Scikit-Image blob detection algorithm.^[77] Qualitative images of the dried drops were obtained by etching with sodium hydroxide the CR39s irradiated at the highest neutron fluence and collected the images with the same microscope.

For the in vitro BNCT experiments, rat osteosarcoma UMR-106 cells (Sigma ECACC, UK) were grown in T75 flasks at $37 \text{ }^\circ\text{C}$ humidified air ($5\% \text{ CO}_2$), in DMEM high glucose (EuroClone S.p.A.), supplemented with 10% (v/v) FBS (Biowest SAS) and $40 \text{ } \mu\text{g mL}^{-1}$ gentamicin (EuroClone S.p.A.). The irradiation was performed on continuously growing non-confluent cell populations by seeding cells 48 h before exposure to the NPs at the density of 1.5×10^6 . Cells were incubated for 18 h with 0.76 mg mL^{-1} (final concentration) of 350 Da PEG-Au-B NPs by diluting 0.5 mL of NPs solution in 9.5 mL of culture medium. After 18 h, the medium with NPs was removed, cells were washed three times with PBS (Euroclone S.p.A.), fresh medium was added, and flasks were subjected to irradiation at 10 or 250 kW of irradiation power for $10'$. For survival rate evaluation, performed by the plating assay, after serial dilutions, cells were plated at two different concentrations (50 – 100 cells per Petri) in five replicate Petri dishes and allowed to grow at $37 \text{ }^\circ\text{C}$ for ten days. Subsequently, colonies were fixed in 70% ethanol, stained with Toluidine blue, and counted. The ratio between the number of colonies with more than fifty cells and the number of seeded cells gave the value of the plating efficiency (PE). The cell survival was obtained by dividing the PE of the treated samples by the PE of the control sample.

Boron concentration was evaluated by neutron autoradiography on aliquots of 4×10^6 cells, previously enriched by centrifugation and then layered on mylar disks to undergo dehydration before being faced on CR39 slides. Irradiation was carried out as explained above for the quantitative measurements. The analysis was performed on 40 sequential pictures, each of 0.3 mm^2 .

CT and XRT Experiments: For CT imaging, phantoms were prepared in a 96 wells plate by serial dilutions, starting from 350 Da PEG-Au-B NPs solutions with a concentration of $4.0 \pm 0.2 \text{ mg Au mL}^{-1}$. CT images were acquired using a small-animal CT system (x-rad, SmART, Precision X-ray) at the following acquisition parameters: tube tension 80 kVp , current 3 mA , 300 views, 0.1 mm voxel size. Images were acquired in triplicate and then reconstructed using the Feldkamp algorithm for cone beam CT, and ImageJ was used to estimate the X-ray attenuation as HU in the phantom volumes based on the intensity of water (normalized to $\text{HU} = 0$). X-ray

attenuation ability in HU mL mg⁻¹ Au was calculated from the slopes of the best-fit lines of HU versus gold concentration.

In clonogenic experiments for XRT, PC3 cells were seeded in triplicate wells at 4×10^3 cells per well and left overnight in the incubator. Then, the medium was removed, and 350 Da PEG-Au-B NPs were incubated at 50 µg mL⁻¹ in 100 µL of medium per well. After 24 h, the medium with NPs was removed, cells were washed with PBS and fresh warm PBS was added. Then, the plates were irradiated at 2 or 4 Gy. After irradiation, cells were detached from the plates using a standard protocol with trypsin and each condition was counted separately using an automated counter (BioRad T10 Automated Cell Counter). Then, each group was plated in triplicate with 500 cells per well in a 6-wells plate, using 2 mL of medium per well. After 8 days in the incubator, plates were coded for a blinded count, then colonies were stained after medium removal using 0.5 mL per well of a crystal violet solution (0.1% crystal violet, 11% ethanol). After 5 min, the staining solution was removed, and plates were rinsed by immersion in water and left to dry at room temperature. Colonies were then counted, and the relative survival fraction was calculated relative to the controls (which were sham irradiated). Results were shown in terms of means ± SE of three independent experiments.

DFT Calculations: The DFT calculations were performed with the QuantumESPRESSO package^[89] using $2 \times 2 \times 2$ supercells containing 32 FCC sites. Wavefunctions were expanded over a plane wave basis set, exchange and correlation were treated through the PBE^[90] functional, and pseudopotentials from the GBRV library^[91] were adopted. Integration over the Brillouin zone was discretized using a $6 \times 6 \times 6$ k-point mesh. Formation energies E_{form} were computed as the difference between the alloy energy and the sum of energies of atomic constituents in their bulk elements.

Substitutional alloy models were special quasirandom structures built using a cluster expansion approach as implemented in ICET. Segregated alloy models were obtained by starting from a distribution of the B atoms within the Au vacancy. Cells and atomic positions of all models were optimized until energy changes were lower than 10^{-4} Ry, forces acting on atoms were lower than 10^{-3} Ry bohr⁻¹, and pressure was lower than 0.5 Kbar.

Statistical Analysis: In the in vitro biocompatibility assays all values were given as mean ± standard deviation (SD) obtained from four independent experiments. At first, the normality of the data was tested using the Shapiro–Wilk test. Two-way ANOVA with Tukey's multiple comparison post-test was subsequently performed. The values of $p < 0.05$ were considered to be statistically significant. The analyses were performed with GraphPad Prism 8 (GraphPad Software, La Jolla, CA, USA).

Data from in vitro survival analysis of each independent irradiation experiment was analyzed in terms of the ratio between treated/control, in which control was sham-irradiated and not incubated with NPs. The means ± standard error (SE) of three independent experiments was shown as the results. The normality test was performed (all groups did not reject normality) prior to the one-way ANOVA analysis to identify statistical significance among data with $p = 0.05$.

Preprocessing of CT data was performed by searching for outliers (none found) and normalizing the data by subtracting all values by the mean Au values of water. Linear fitting was performed using the means ± SE of the data ($N = 3$) and Y error as weight, with no fixed parameters.

All processing was performed using Origin software (OriginLab, USA).

Supporting Information

Supporting Information is available from the Wiley Online Library or from the author.

Acknowledgements

The authors acknowledge the support from the University of Padova P-DiSC grant DYNAMO and from AIRC under MFAG 2021-ID. 25681 project – P.I. A.V., the European Synchrotron Radiation Facility (ESRF) for provision of synchrotron radiation facilities, the Computational Chemistry

Community (C3P) of the University of Padova, the Serbian Ministry of Science, Technological Development and Innovation (Contract No. 451-03-47/2023-01/200019) and the Serbian Academy of Sciences and Arts project F115. Dr. Francesco D'Acapito is acknowledged for assistance and support in using beamline BM08.

Conflict of Interest

The authors declare no conflict of interest.

Data Availability Statement

The data that support the findings of this study are available from the corresponding author upon reasonable request.

Keywords

alloys, boron neutron capture therapy (BNCT), computed tomography (CT), laser-synthesis, X-ray radiotherapy (XRT)

Received: March 26, 2023

Revised: May 17, 2023

Published online: June 20, 2023

- [1] J. Shi, P. W. Kantoff, R. Wooster, O. C. Farokhzad, *Nat. Rev. Cancer* **2017**, *17*, 20.
- [2] B. Youden, R. Jiang, A. J. Carrier, M. R. Servos, X. Zhang, *ACS Nano* **2022**, *16*, 17497.
- [3] Q. Sun, Z. Zhou, N. Qiu, Y. Shen, *Adv. Mater.* **2017**, *29*, 1606628.
- [4] I. Roy, S. Krishnan, A. V. Kabashin, I. N. Zavestovskaya, P. N. Prasad, *ACS Nano* **2022**, *16*, 5036.
- [5] G. Yang, S. Z. F. Phua, A. K. Bindra, Y. Zhao, *Adv. Mater.* **2019**, *31*, 1805730.
- [6] D. M. Valcourt, C. H. Kapadia, M. A. Scully, M. N. Dang, E. S. Day, *Adv. Healthcare Mater.* **2020**, *9*, 2000110.
- [7] Z. Zhou, K. Hu, R. Ma, Y. Yan, B. Ni, Y. Zhang, L. Wen, Q. Zhang, Y. Cheng, *Adv. Funct. Mater.* **2016**, *26*, 5971.
- [8] X.-R. Song, S.-X. Yu, G.-X. Jin, X. Wang, J. Chen, J. Li, G. Liu, H.-H. Yang, *Small* **2016**, *12*, 1506.
- [9] T. Shanmugasundaram, M. Radhakrishnan, V. Gopikrishnan, K. Kadirvelu, R. Balagurunathan, *Nanoscale* **2017**, *9*, 16773.
- [10] Y. Chong, J. Huang, X. Xu, C. Yu, X. Ning, S. Fan, Z. Zhang, *Bioconjugate Chem.* **2020**, *31*, 1756.
- [11] B. S. Ahmed, A. G. Rao, B. M. Sankarshan, C. S. Vicas, K. Namratha, T. K. Umesh, R. Somashekar, K. Byrappa, *Cancer Oncol. Res.* **2016**, *4*, 42.
- [12] V. Amendola, S. Scaramuzza, L. Litti, M. Meneghetti, G. Zuccolotto, A. Rosato, E. Nicolato, P. Marzola, G. Fracasso, C. Anselmi, M. Pinto, M. Colombatti, *Small* **2014**, *10*, 2476.
- [13] V. Torresan, D. Forrer, A. Guadagnini, D. Badocco, P. Pastore, M. Casarin, A. Selloni, D. Coral, M. Ceolin, M. B. Fernández van Raap, A. Busato, P. Marzola, A. E. Spinelli, V. Amendola, *ACS Nano* **2020**, *14*, 12840.
- [14] E. B. Ehlerding, F. Chen, W. Cai, *Adv. Sci.* **2016**, *3*, 1500223.
- [15] V. Amendola, A. Guadagnini, S. Agnoli, D. Badocco, P. Pastore, G. Fracasso, M. Gerosa, F. Vurro, A. Busato, P. Marzola, *J. Colloid Interface Sci.* **2021**, *596*, 332.
- [16] X. Wang, W. Yao, R. Guo, X. Yang, J. Tang, J. Zhang, W. Gao, V. Timchenko, J. Liu, *Adv. Healthcare Mater.* **2018**, *7*, 1800318.

- [17] K. O. Aiyzyzh, E. V. Barmina, V. V. Voronov, G. A. Shafeev, G. G. Novikov, O. V. Uvarov, *Opt. Laser Technol.* **2022**, *155*, 108393.
- [18] A. I. Pastukhov, I. B. Belyaev, J. C. Bulmahn, I. V. Zelepukin, A. A. Popov, I. N. Zvestovskaya, S. M. Klimentov, S. M. Deyev, P. N. Prasad, A. V. Kabashin, *Sci. Rep.* **2022**, *12*, 9129.
- [19] M. Laprise-Pelletier, T. Simão, M.-A. Fortin, *Adv. Healthcare Mater.* **2018**, *7*, 1701460.
- [20] A. M. Hughes, *Expert Rev. Mol. Med.* **2022**, *24*, e14.
- [21] K. R. Pulagam, M. Henriksen-Lacey, K. B. Uribe, C. Renero-Lecuna, J. Kumar, A. Charalampopoulou, A. Facoetti, N. Protti, V. Gómez-Vallejo, Z. Baz, V. Kumar, A. Sánchez-Iglesias, S. Altieri, U. Cossío, D. Di Silvio, A. M. Martínez-Villacorta, A. Ruiz De Angulo, L. Rej, C. M. Liz-Marzán, J. Llop, *ACS Appl. Mater. Interfaces* **2021**, *13*, 49589.
- [22] Q. Dai, Q. Yang, X. Bao, J. Chen, M. Han, Q. Wei, *Mol. Pharmaceutics* **2022**, *19*, 363.
- [23] V. Torresan, A. Guadagnini, D. Badocco, P. Pastore, G. A. Muñoz Medina, M. B. Fernández van Raap, I. Postuma, S. Bortolussi, M. Bekić, M. Čolić, M. Gerosa, A. Busato, P. Marzola, V. Amendola, *Adv. Healthcare Mater.* **2020**, *10*, 2001632.
- [24] G. Ailuno, A. Balboni, G. Caviglioli, F. Lai, F. Barbieri, I. Dellacasagrande, T. Florio, S. Baldassari, *Cells* **2022**, *11*, 4029.
- [25] T. D. Malouff, D. S. Seneviratne, D. K. Ebner, W. C. Stross, M. R. Waddle, D. M. Trifletti, S. Krishnan, *Front. Oncol.* **2021**, *11*, 351.
- [26] H. Koivunoro, S. González, L. Provenzano, G. S. Cruz, L. Kankaanranta, S. Savolainen, H. Joensuu, *Radiother. Oncol.* **2016**, *118*, S58.
- [27] L.-W. Wang, Y.-W. H. Liu, F.-I. Chou, S.-H. Jiang, *Cancer Commun.* **2018**, *38*, 37.
- [28] A. Zonta, T. Pinelli, U. Prati, L. Roveda, C. Ferrari, A. M. Clerici, C. Zonta, G. Mazzini, P. Dionigi, S. Altieri, S. Bortolussi, P. Bruschi, F. Fossati, *Appl. Radiat. Isot.* **2009**, *67*, S67.
- [29] M. Sasai, H. Nakamura, N. Sougawa, Y. Sakurai, M. Suzuki, C. M. Lee, *Anticancer Res.* **2016**, *36*, 907.
- [30] R. F. Barth, J. C. Grecula, *Appl. Radiat. Isot.* **2020**, *160*, 109029.
- [31] T. Nomoto, N. Nishiyama, *Biomaterials* **2018**, *178*, 583.
- [32] S. Savolainen, M. Kortensniemi, M. Timonen, V. Reijonen, L. Kuusela, J. Uusi-Simola, E. Salli, H. Koivunoro, T. Seppälä, N. Lönnroth, P. Välimäki, H. Hyvönen, P. Kotiluoto, T. Serén, A. Kuronen, S. Heikkinen, A. Kosunen, I. Auterinen, *Phys. Medica* **2013**, *29*, 233.
- [33] K. Takada, H. Kumada, A. Matsumura, H. Sakurai, T. Sakae, *Appl. Radiat. Isot.* **2020**, *165*, 109295.
- [34] S.-I. Miyatake, S. Kawabata, R. Hiramatsu, T. Kuroiwa, M. Suzuki, N. Kondo, K. Ono, *Neurol. Med. Chir.* **2016**, *56*, 361.
- [35] Y. Ariyoshi, M. Shimahara, Y. Kimura, Y. Ito, T. Shimahara, S.-I. Miyatake, S. Kawabata, *Oncol. Lett.* **2011**, *2*, 423.
- [36] T. Morita, H. Kurihara, K. Hiroi, N. Honda, H. Igaki, J. Hatazawa, Y. Arai, J. Itami, *Radiat. Oncol.* **2018**, *13*, 4.
- [37] T. Yamamoto, K. Nakai, T. Nariiai, H. Kumada, T. Okumura, M. Mizumoto, K. Tsuboi, A. Zaboronok, E. Ishikawa, H. Aiyama, K. Endo, T. Takada, F. Yoshida, Y. Shibata, A. Matsumura, *Appl. Radiat. Isot.* **2011**, *69*, 1817.
- [38] J. C. Lee, K. S. Chuang, Y. W. H. Liu, T. Y. Lin, Y. C. Teng, L. W. Wang, *PLoS One* **2019**, *14*, e0210626.
- [39] K. Haume, S. Rosa, S. Grellet, M. A. Śmiątek, K. T. Butterworth, A. V. Solov'yov, K. M. Prise, J. Golding, N. J. Mason, *Cancer Nanotechnol.* **2016**, *7*, 8.
- [40] A. A. Lipengolts, Y. A. Finogenova, V. A. Skribitsky, E. Y. Grigorieva, *J. Phys.: Conf. Ser.* **2021**, *2058*, 012039.
- [41] S. J. McMahon, H. Paganetti, K. M. Prise, *Nanoscale* **2015**, *8*, 581.
- [42] U. M. Cytlak, D. P. Dyer, J. Honeychurch, K. J. Williams, M. A. Travis, T. M. Illidge, *Nat. Rev. Immunol.* **2021**, *22*, 124.
- [43] N. Kuthala, M. Shanmugam, C. L. Yao, C. S. Chiang, K. C. Hwang, *Biomaterials* **2022**, *290*, 121861.
- [44] J. Jo, J. Folz, M. E. Gonzalez, A. Paoli, A. Eido, E. Salfi, S. Tekula, S. Andò, R. Caruso, C. G. Kleer, X. Wang, R. Kopelman, *ACS Nano* **2023**, *17*, 4396.
- [45] D. Kim, J. Kim, Y. Il Park, N. Lee, T. Hyeon, *ACS Cent. Sci.* **2018**, *4*, 324.
- [46] X. Han, K. Xu, O. Taratula, K. Farsad, *Nanoscale* **2019**, *11*, 799.
- [47] H. Okamoto, *Desk Handbook: Phase Diagrams for Binary Alloys*, ASM International, Materials Park, OH, **2000**.
- [48] V. Amendola, D. Amans, Y. Ishikawa, N. Koshizaki, S. Scirè, G. Compagnini, S. Reichenberger, S. Barcikowski, *Chem. - Eur. J.* **2020**, *26*, 9206.
- [49] J. Theerthagiri, K. Karuppasamy, S. J. Lee, R. Shwetharani, H. S. Kim, S. K. K. Pasha, M. Ashokkumar, M. Y. Choi, *Light Sci. Appl.* **2022**, *11*, 250.
- [50] D. Zhang, B. Gökce, S. Barcikowski, *Chem. Rev.* **2017**, *117*, 3990.
- [51] S. Jendrzej, B. Gökce, M. Eppe, S. Barcikowski, *ChemPhysChem* **2017**, *18*, 1012.
- [52] S. Crivellaro, A. Guadagnini, D. M. D. M. Arboleda, D. Schinca, V. Amendola, *Rev. Sci. Instrum.* **2019**, *90*, 033902.
- [53] V. Amendola, M. Meneghetti, *Phys. Chem. Chem. Phys.* **2013**, *15*, 3027.
- [54] A. Guadagnini, S. Agnoli, D. Badocco, P. Pastore, R. Pilot, R. Ravelle-Chapuis, M. B. F. Raap, V. Amendola, *ChemPhysChem* **2021**, *22*, 657.
- [55] S. Scaramuzza, S. Polizzi, V. Amendola, *Nanoscale Adv.* **2019**, *1*, 2681.
- [56] T. L. Doane, C. H. Chuang, R. J. Hill, C. Burda, *Acc. Chem. Res.* **2011**, *45*, 317.
- [57] D. T. L. Alexander, D. Forrer, E. Rossi, E. Lidorikis, S. Agnoli, G. D. Bernasconi, J. Butet, O. J. F. Martin, V. Amendola, *Nano Lett.* **2019**, *19*, 5754.
- [58] V. Amendola, S. Scaramuzza, S. Agnoli, G. Granozzi, M. Meneghetti, G. Campo, V. Bonanni, F. Pineider, C. Sangregorio, P. Ghigna, S. Fiameni, L. Nodari, S. Polizzi, P. Riello, S. Fiameni, L. Nodari, *Nano Res.* **2015**, *8*, 4007.
- [59] V. Amendola, S. Scaramuzza, S. Agnoli, S. Polizzi, M. Meneghetti, *Nanoscale* **2014**, *6*, 1423.
- [60] V. Amendola, M. Meneghetti, O. M. Bakr, P. Riello, S. Polizzi, S. Fiameni, H. Dalaver, P. Arosio, T. Orlando, C. de Julian Fernandez, F. Pineider, C. Sangregorio, A. Lascialfari, *Nanoscale* **2013**, *5*, 5611.
- [61] C. Bravin, V. Amendola, *ACS Appl. Nano Mater.* **2022**, *5*, 578.
- [62] M. Carmen Bautista, O. Bomati-Miguel, M. Del Puerto Morales, C. J. Serna, S. Veintemillas-Verdaguer, *J. Magn. Magn. Mater.* **2005**, *293*, 20.
- [63] R. Choi, J. Yang, J. Choi, E. K. Lim, E. Kim, J. S. Suh, Y. M. Huh, S. Haam, *Langmuir* **2010**, *26*, 17520.
- [64] D. G. Castner, K. Hinds, D. W. Grainger, *Langmuir* **1996**, *12*, 5083.
- [65] W. L. Dai, H. X. Li, Y. Cao, M. H. Qiao, K. N. Fan, J. F. Deng, *Langmuir* **2002**, *18*, 9605.
- [66] C. W. Ong, H. Huang, B. Zheng, R. W. M. Kwok, Y. Y. Hui, W. M. Lau, *J. Appl. Phys.* **2004**, *95*, 3527.
- [67] H. Li, X. Qin, X. G. Zhang, K. Jiang, W. B. Cai, *ACS Catal.* **2022**, *12*, 12750.
- [68] F. Pineider, C. De Julián Fernández, V. Videtta, E. Carlino, A. Al Hourani, F. Wilhelm, A. Rogalev, P. D. Cozzoli, P. Ghigna, C. Sangregorio, *ACS Nano* **2013**, *7*, 857.
- [69] F. Bonaccorso, M. Zerbetto, A. C. C. Ferrari, V. Amendola, *J. Phys. Chem. C* **2013**, *117*, 13217.
- [70] V. Coviello, D. Forrer, V. Amendola, *ChemPhysChem* **2022**, *23*, 202200136.
- [71] A. Guadagnini, S. Agnoli, D. Badocco, P. Pastore, D. Coral, M. B. Fernández van Raap, D. Forrer, V. Amendola, *J. Colloid Interface Sci.* **2021**, *585*, 267.
- [72] L. Ciani, S. Bortolussi, I. Postuma, L. Cansolino, C. Ferrari, L. Panza, S. Altieri, S. Ristori, *Int. J. Pharm.* **2013**, *458*, 340.

- [73] J. Blechinger, A. T. Bauer, A. A. Torrano, C. Gorzelanny, C. Brauchle, S. W. Schneider, *Small* **2013**, *9*, 3970.
- [74] S. Tomić, J. Dokić, S. Vasilijić, N. Ogrinc, R. Rudolf, P. Pelicon, D. Vučević, P. Milosavljević, S. Janković, I. Anžel, J. Rajković, M. S. Rupnik, B. Friedrich, M. Čolić, *PLoS One* **2014**, *9*, e96584.
- [75] M. Bekić, S. Tomić, R. Rudolf, M. Milanović, D. Vučević, I. Anžel, M. Čolić, *Materials* **2019**, *12*, 4121.
- [76] A. Zaboronok, P. Khaptakhanova, S. Uspenskii, R. Bekarevich, L. Mechetina, O. Volkova, B. J. Mathis, V. Kanygin, E. Ishikawa, A. Kasatova, D. Kasatov, I. Shchudlo, T. Sycheva, S. Taskaev, A. Matsumura, *Pharmaceutics* **2022**, *14*, 761.
- [77] I. Postuma, S. Bortolussi, N. Protti, F. Ballarini, P. Bruschi, L. Ciani, S. Ristori, L. Panza, C. Ferrari, L. Cansolino, S. Altieri, *Rep. Pract. Oncol. Radiother.* **2016**, *21*, 123.
- [78] A. M. D. Viegas, I. Postuma, S. Bortolussi, C. Guidi, J. S. Riback, L. Provenzano, B. Marcaccio, A. E. Rossini, C. Ferrari, L. Cansolino, M. Ferrari, A. M. Portu, S. J. González, *Phys. Medica* **2021**, *89*, 282.
- [79] S. Bortolussi, I. Postuma, N. Protti, L. Provenzano, C. Ferrari, L. Cansolino, P. Dionigi, O. Galasso, G. Gasparini, S. Altieri, S. I. Miyatake, S. J. González, *Radiat. Oncol.* **2017**, *12*, 130.
- [80] K. Hirose, A. Konno, J. Hiratsuka, S. Yoshimoto, T. Kato, K. Ono, N. Otsuki, J. Hatazawa, H. Tanaka, K. Takayama, H. Wada, M. Suzuki, M. Sato, H. Yamaguchi, I. Seto, Y. Ueki, S. Iketani, S. Imai, T. Nakamura, T. Ono, H. Endo, Y. Azami, Y. Kikuchi, M. Murakami, Y. Takai, *Radiother. Oncol.* **2021**, *155*, 182.
- [81] Y. W. Chen, Y. Y. Lee, C. F. Lin, P. S. Pan, J. K. Chen, C. W. Wang, S. M. Hsu, Y. C. Kuo, T. L. Lan, S. P. C. Hsu, M. L. Liang, R. H. H. Chen, F. C. Chang, C. C. Wu, S. C. Lin, H. K. Liang, J. C. Lee, S. K. Chen, H. M. Liu, J. J. Peir, K. H. Lin, W. S. Huang, K. H. Chen, Y. M. Kang, S. C. Liou, C. C. Wang, P. C. Pai, C. W. Li, D. Q. S. Chiek, T. T. Wong, *Exp. Biol. Med.* **2021**, *10*, 334.
- [82] X. Duan, J. Wang, L. Yu, S. Leng, C. H. McCollough, *Med. Phys.* **2011**, *38*, 993.
- [83] NIST, <http://physics.nist.gov/PhysRefData/XrayMassCoef/tab3.html> (accessed: January 2023).
- [84] Z. Miao, S. Chen, C. Y. Xu, Y. Ma, H. Qian, Y. Xu, H. Chen, X. Wang, G. He, Y. Lu, Q. Zhao, Z. Zha, *Chem. Sci.* **2019**, *10*, 5435.
- [85] A. Xia, M. Chen, Y. Gao, D. Wu, W. Feng, F. Li, *Biomaterials* **2012**, *33*, 5394.
- [86] J. Xie, L. Gong, S. Zhu, Y. Yong, Z. Gu, Y. Zhao, *Adv. Mater.* **2019**, *31*, 1802244.
- [87] X. Hu, T. Björkman, H. Lipsanen, L. Sun, A. V. Krashennikov, *J. Phys. Chem. Lett.* **2015**, *6*, 3263.
- [88] T. Chen, I. Ellis, T. J. N. Hooper, E. Liberti, L. Ye, B. T. W. Lo, C. O'Leary, A. A. Sheader, G. T. Martinez, L. Jones, P. L. Ho, P. Zhao, J. Cookson, P. T. Bishop, P. Chater, J. V. Hanna, P. Nellist, S. C. Edman Tsang, *J. Am. Chem. Soc.* **2019**, *141*, 19616.
- [89] P. Giannozzi, O. Andreussi, T. Brumme, O. Bunau, M. Buongiorno Nardelli, M. Calandra, R. Car, C. Cavazzoni, D. Ceresoli, M. Cococcioni, N. Colonna, I. Carnimeo, A. Dal Corso, S. de Gironcoli, P. Delugas, R. A. DiStasio, A. Ferretti, A. Floris, G. Fratesi, G. Fugallo, R. Gebauer, U. Gerstmann, F. Giustino, T. Gorni, J. Jia, M. Kawamura, H.-Y. Ko, A. Kokalj, E. Küçükbenli, M. Lazzeri, et al., *J. Phys.: Condens. Matter* **2017**, *29*, 465901.
- [90] J. P. Perdew, K. Burke, M. Ernzerhof, *Phys. Rev. Lett.* **1996**, *77*, 3865.
- [91] K. F. Garrity, J. W. Bennett, K. M. Rabe, D. Vanderbilt, *Comput. Mater. Sci.* **2014**, *81*, 446.